scientific reports

Check for updates

OPEN

Breast tumor segmentation in ultrasound using distance-adapted fuzzy connectedness, convolutional neural network, and active contour

Marta Biesok✉, Jan Juszczyk & Pawel Badura

This study addresses computer-aided breast cancer diagnosis through a hybrid framework for breast tumor segmentation in ultrasound images. The core of the three-stage method is based on the autoencoder convolutional neural network. In the first stage, we prepare a hybrid pseudo-color image through multiple instances of fuzzy connectedness analysis with a novel distance-adapted fuzzy affinity. We produce different weight combinations to determine connectivity maps driven by particular image specifics. After the hybrid image is processed by the deep network, we adjust the segmentation outcome with the Chan-Vese active contour model. We find the idea of incorporating fuzzy connectedness into the input data preparation for deep-learning image analysis our main contribution to the study. The method is trained and validated using a combined dataset of 993 breast ultrasound images from three public collections frequently used in recent studies on breast tumor segmentation. The experiments address essential settings and hyperparameters of the method, e.g., the network architecture, input image size, and active contour setup. The tumor segmentation reaches a median Dice index of 0.86 (mean at 0.79) over the combined database. We refer our results to the most recent state-of-the-art from 2022–2023 using the same datasets, finding our model comparable in segmentation performance.

Keywords Breast cancer, Ultrasound, Breast tumor segmentation, Fuzzy connectedness, Convolutional neural networks, Active contours

Cancer is the leading cause of death in developed countries and the second leading cause in developing countries[1], with breast cancer being one of the deadliest in women[2]. Among breast cancer types, invasive ductal carcinoma (IDC) and invasive lobular carcinoma (ILC) are the most common[3]. Breast cancer can metastasize to other body parts by invading blood vessels or lymph nodes[4]. According to the American Cancer Society, approximately 288,000 cases of invasive breast cancer were diagnosed in women and 2710 in men in the United States in 2022 alone[2]. Over four million people live in the US with breast cancer diagnoses, with over 150,000 cases with metastases to other organs. Thus, one in eight women is expected to develop breast cancer, and the risk increases with age. A similar relationship appears in mortality data: from less than 0.1% in young women (20–30 years old) to about 1% in women over 80. In Poland, breast cancer covered 23.8% of all female cancers in 2020, while in men, it was just 0.2%[5].

The key to successful breast cancer therapy is to detect the lesion early[6], increasing the chance of complete recovery and breast-conserving surgery. The survival rate in small tumors and no metastases exceeds 90%[7]. Screening tests that detect lesions before they are palpable have become common in developed countries. The examinations most frequently used in Poland involve mammography or ultrasound (US)[8]. The latter has the highest diagnostic accuracy distinguishing between a solid tumor and a cyst, yet it does not detect microcalcifications typical in early-stage breast cancer[9].

US imaging measures the emitted ultrasound wave echo after reflection from internal body structures and produces a so-called B-scan (brightness)[10]. Its main advantages lie in widespread availability, intraoperative real-time imaging capability, and lack of ionizing radiation[11,12]. On the other hand, US scans require experience

Faculty of Biomedical Engineering, Silesian University of Technology, Roosevelta 40, 41-800 Zabrze, Poland. ✉email: marta.biesok@polsl.pl

in acquisition and interpretation and are noisier than, e.g., computed tomography or magnetic resonance projections. A US-guided breast biopsy is a standard procedure in mammary gland diagnosis[13]. Since the biopsy needle is trackable in real-time, the tissue sample can be taken from a specific location near the tumor[14,15].

Sample US images of breast tumors are presented in Fig. 1. Tumor appearance differs significantly in various types. Solid tumors are hyperechogenic, i.e., they reflect ultrasound waves strongly and appear as bright. On the other hand, cysts and soft tumors are hypoechogenic (darker than the surrounding tissues). Malignancy can also be assessed in US. Benign breast tumors tend to be regular in shape with soft edges, while malignant tumors have irregular contours and various forms. The tumor shape analysis in US often suffers from so-called acoustic shadows, i.e., areas hidden behind structures strongly reflecting the US waves. Diffraction blurs the edges of the acoustic shadow, making the tumor shape and size assessment challenging. The lower lesion boundary estimation relies on the expert's experience in such cases. This is one of the reasons why computer-aided diagnosis (CAD) based on US images is a significant challenge. Artificial intelligence can help by learning to recognize textures and shapes with incomplete boundaries[16]. The latter statement certainly concerns image segmentation, often the first and crucial stage in CAD: dividing the image into semantically homogeneous areas based on selected criteria[17]. The recent decade brought a staggering development of deep learning methods[18,19], also for image segmentation, and breast lesion analysis is no exception here. Deep neural networks contain many layers and neurons controlled by millions of trainable parameters. Whole images are inputted into the models for training and analysis through multiscale processing.

Before the expansion of deep learning approaches, breast tumors were extracted in US scans using various canonical methods based on thresholding, watersheds, graphs, clustering, active contours, region analysis, Markov random fields, and classical neural networks (valuable surveys can be found in[21,22]), but their efficiency was limited and ought to be addressed in high-noise images[23]. The current state-of-the-art segmentation methods are concentrated around deep networks[24–31]. Almajalid et al.[24] employed a U-Net convolutional neural network (CNN) with some pre- and postprocessing and obtained a Dice similarity coefficient (Dice index) of 0.83 over a private set of 221 images. The attention-enriched U-Net model proposed by Vakanski et al.[25] produced a Dice index of 0.90 over a private collection with 510 cases.

The studies described above mostly used their own breast US datasets, yet there are several public benchmark collections with hundreds of images each, willingly employed by recent research. Three of them have also been used in this study: BUSI[20], Dataset B[32], and OASBUD[33] (they are described in detail in "Materials" Section). Shareef et al.[26] prepared a U-Net-like STAN architecture dedicated to small tumors. They reported a Dice index at 0.78 over Dataset B and 0.91 in another BUSIS database[34]. Huang et al.[27] combined fuzzy logic with the CNN. In their SCFURNet model, they equipped a U-Net architecture with spatial-wise and channel-wise fuzzy blocks for uncertainty reduction, yielding a Dice index of 0.81 in both BUSI and Dataset B (plus 0.93 in BUSIS database and 0.82 in a multiclass task over a private collection). The hybrid attentional guidance HAG-Net model from Lu et al.[28] used a multiscale guidance block to extract low-resolution lesion location data and a short multi-head self-attention with convolutional block attention module to analyze global features and long-range dependencies. The Dice index reached 0.83 in BUSI and 0.78 in OASBUD. Chen[29]prepared a refinement residual convolutional network RRCNet. The SegNet model produced coarse saliency maps, refined later by missed-detection and false-detection residual networks. The Dice index was 0.79 in BUSI and 0.80 in Dataset Yang et al.[30] designed a transformer-type pyramid network CSwin-PNet with an attention mechanism. The encoder-decoder architecture was supported by interactive channel attention modules, supplementary feature fusion modules, and additional boundary detectors. They obtained noticeable levels of the Dice index: 0.84 in BUSI and 0.87 in Dataset Ru et al.[31] were the only team that employed all three public collections mentioned here, obtaining the Dice index of 0.77 in BUSI, 0.78 in Dataset B, and 0.60 in OASBUD (note that the Dice index over the other two datasets was 0.70 each). Their approach, Att-U-Node, was based on a U-Net architecture with neural ordinary differential equation blocks and attention modules.

In this paper, we propose a hybrid method for breast tumor segmentation in US based on an autoencoder convolutional neural network supported by fuzzy connectedness (FC) and active contour (AC). At the preprocessing stage, the input image is subjected to the FC analysis with a novel distance-related fuzzy affinity function with various settings. Two obtained fuzzy connectivity scenes are combined with the original scan in a hybrid pseudo-RGB image. The CNN performs its segmentation, and the result constitutes the initial contour in AC-based postprocessing. We employ three public databases[20,32,33] to assess the methodology in multiple experiments on various settings and parameters and compare our performance to the state-of-the-art. The

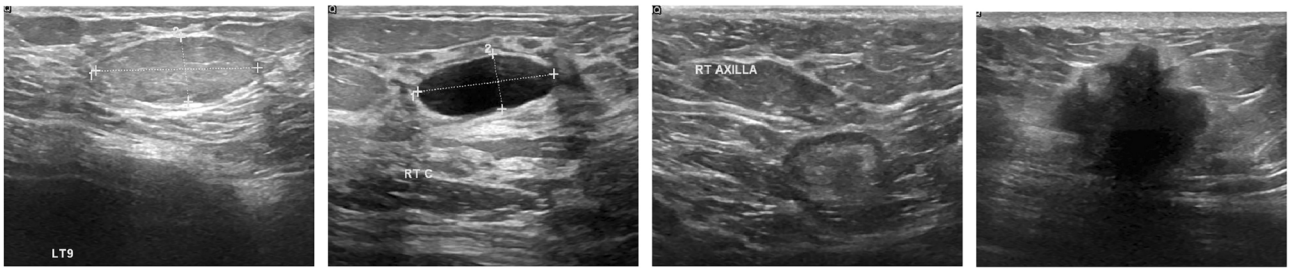

(a) benign, hyperechogenic **(b)** benign, hypoechogenic **(c)** malignant, hyperechogenic **(d)** malignant, hypoechogenic

Fig. 1. Sample ultrasound images with breast tumors[20].

novelty of the study can primarily be found in incorporating fuzzy connectedness into the data preparation for deep-learning semantic segmentation. We discuss the possible benefits of FC for deep medical image analysis in "Discussion" Section.

After the introduction in "Introduction" Section, we specify the materials and methods in "Materials and methods" Section: three reference US image databases and the entire three-stage segmentation methodology. "Results and discussion" Section addresses four experiments on our framework, a comparative analysis to the state-of-the-art, and a discussion of the study. The conclusion is given in "Conclusion" Section.

Materials and methods

Materials

Our experimental image data come from three sources:

1. The BUSI dataset, published by Cairo University in 2019, is public and available online https://doi.org/10.1016/j.dib.2019.104863[20]. The images come from 600 patients aged 25–75, recorded in 2018 at Baheya Hospital in Giza, Egypt, using the LOGIQ E9 US system and the LOGIQ E9 Agile US system with the ML6-15-D Matrix linear transducer (1–5 MHz). The database contains 780 images of approximately $500\times$ 500 pixels in three classes: benign tumors (487), malignant tumors (210), and healthy tissue (133). The expert delineation is available for each image. In this study, we employ only images with a single benign or malignant lesion, limiting the collection size to 630 images.
2. Dataset B, resulting from an international collaboration of scientists from Great Britain, Sudan, and Spain[32]. Dataset B can be accessed for research at the request. It contains 163 images of various resolutions (average of 760×570 pixels) with 110 benign and 53 malignant tumors with expert delineations. The images were acquired using a Siemens ACUSON Sequoia C512 camera with a 17L5 HD linear transducer (frequency 8.5 MHz).
3. The OASBUD dataset, published by the Polish Academy of Sciences in 2017, available http://bluebox.ippt.gov.pl/%7ehpiotrzk/download.html[33]. It includes 100 cases from 78 women (52 malignant and 48 benign tumors). Each lesion was imaged by two perpendicular US scans using an Ultrasonix SonixTouch Research scanner with an L14-5/38 linear transducer (10 MHz), yielding 200 images, each outlined by an expert with 18 years of experience.

We selected these datasets due to their public accessibility and intensive use as reference data for breast tumor segmentation in recent years. This enables a quantitative comparison of our method to existing, up-to-date solutions. Combining three datasets gave us a collection of 993 images with significant diversity in terms of sources, research subjects, and acquisition equipment and parameters.

The experiments were performed in Matlab (R2021b version, Image Processing Toolbox, Deep Learning Toolbox, Computer Vision Toolbox) on a workstation with a 12-core AMD Ryzen 9 CPU 3.09 GHz, 32GB RAM, and an NVIDIA TITAN RTX 24GB GPU.

Methods

Figure 2 shows the three-stage breast tumor segmentation workflow proposed in this study. Its details are given in the following sections. The semi-automated method has two inputs: a US image containing a breast tumor and a seed point o located in the center of the lesion. The seed point can be indicated manually by an expert or result from any previous US image analysis.

Preprocessing using modified fuzzy connectedness

The segmentation starts with preparing a hybrid pseudo-color image using fuzzy connectedness analysis. Fuzzy connectedness is a method for determining the level of membership of a pixel or voxel to a selected class or object[35,36]. It relies on determining fuzzy connectivity scenes according to the fuzzy affinity μ_κ linking adjacent pixels. In image analysis, μ_κ considers, e.g., pixel intensity, local gradient, or location[37]. Determination of fuzzy connectivity scenes employs shortest-path graph search, e.g., dynamic programming or Dijkstra's algorithm. The scene can be thresholded to produce binary segmentation, yet we use fuzzy connectivity directly in this study. To support the original image, we calculate two fuzzy connectivity scenes regarding seed point o using a matrix-optimized Dijkstra's search[38]. Then, we combine all three into a pseudo-RGB image with the original US scan placed in the red channel (Fig. 3).

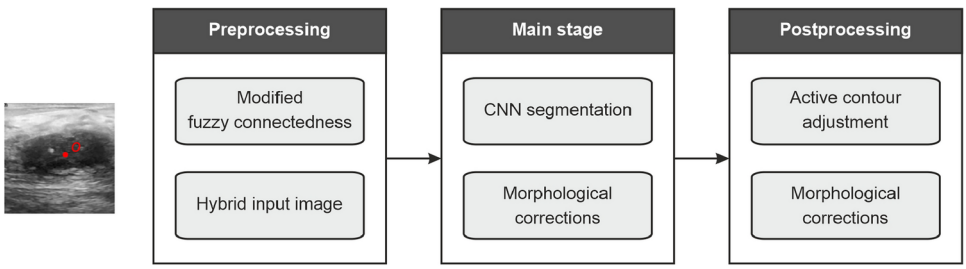

Fig. 2. General breast tumor segmentation workflow.

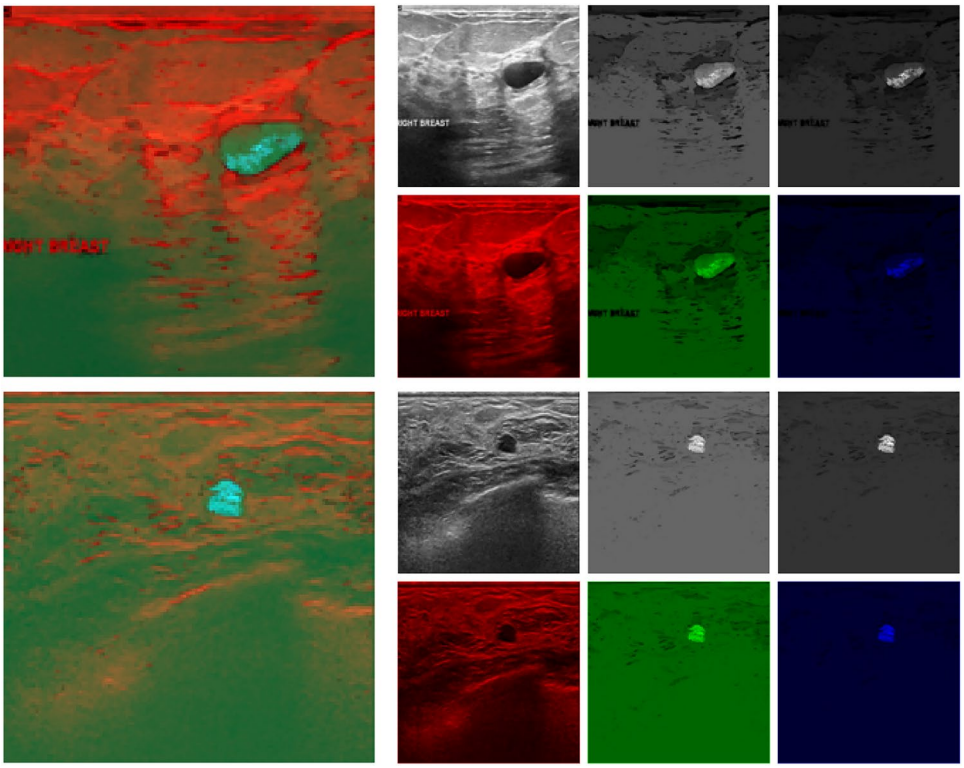

Fig. 3. Illustration of hybrid pseudo-color images. In each of the two cases, the hybrid image is shown on the left, and its components are on the right (left to right: the original US image and two fuzzy connectivity scenes ($\mathbf{W}_1$ and $\mathbf{W}_2$, respectively) as grayscale images above, and mapped to the appropriate chromatic channel below).

Our fuzzy affinity function modifies the original proposed by Udupa et al.[35]:

$$\mu_\kappa(c,d) = w_1 e^{\frac{-0{,}5\left(\frac{(I_c+I_d)}{2}-m_1\right)^2}{s_1^2}} + w_2 e^{\frac{-0{,}5(|I_c-I_d|-m_2)^2}{s_2^2}}, \tag{1}$$

where I_d, I_c are the image intensities of pixels *c* and *d*, respectively, m_1, m_2, s_1, s_2 are intensity-related affinity parameters reflecting the segmented object properties, and w_1, w_2 weigh the influence of the affinity components ($w_1 + w_2 = 1$). μ_κ is nonzero for topologically adjacent pixels *c*, *d* only (here, we use 4-connectivity). Still, such elementary relationships lead along multi-pixel paths to fuzzy connectivities between any point *d* in the image and a seed point *o*.

Our modification of fuzzy affinity considers that the segmented object is compact and occupies a relatively small part of the image in most cases. Thus, we introduce another factor to address the distance between pixel *d* and seed point *o*. We use Euclidean distance:

$$dist(o,d) = \sqrt{(x_o - x_d)^2 + (y_o - y_d)^2}, \tag{2}$$

where x_o, x_d are horizontal coordinates, and y_o, y_d – vertical coordinates of pixels *o* and *d*, respectively. The distance is then normalized to the maximum value:

$$dist_n(o,d) = 1 - \frac{dist(o,d)}{\max\limits_e(dist(o,e))}. \tag{3}$$

We add the distance component to Eq. (1):

$$\mu(c,d) = w_1 e^{\frac{-0{,}5\left(\frac{(I_c+I_d)}{2}-m_1\right)^2}{s_1^2}} + w_2 e^{\frac{-0{,}5(|I_c-I_d|-m_2)^2}{s_2^2}} + w_3 dist_n(o,d). \tag{4}$$

With a new weight w_3, now we have to secure: $w_1 + w_2 + w_3 = 1$.

The distance component should not dominate the others, and we found $w_3 = 0.1$ appropriate for our experiments with relatively noisy US images. Furthermore, to highlight various image features, we proposed two weight vectors $\mathbf{W}_i = [w_1, w_2, w_3]$ applied to Eq. (4) for determining two distinct fuzzy connectivity scenes:

$$\mathbf{W}_1 = [0.8, 0.1, 0.1], \tag{5}$$

$$\mathbf{W}_2 = [0.1, 0.8, 0.1]. \tag{6}$$

The $\mathbf{W}_1$ vector emphasizes mean intensity-related similarity, while $\mathbf{W}_2$ favors gradient similarity. The fuzzy scenes they produce carry different information. Both are combined with the original US scan to the pseudo-RGB image (Fig. 3) and passed as an input to the CNN-based main segmentation stage.

CNN segmentation

For the main stage of the segmentation workflow, we designed an autoencoder CNN architecture (Fig. 4). The network is four levels deep. It is fed with the pseudo-color image, prepared with the modified FC scheme described in "Preprocessing using modified fuzzy connectedness" Section, resampled to a 128×128 size. The experiments presented in "Results and discussion" Section justify our architecture and image size selections.

For training, we employed stochastic gradient descent with momentum (SGDM) with the initial learning rate of 0.1, learning rate drop factor of 0.7, momentum of 0.95, maximum number of epochs of 50, and a generalized Dice loss. The mini-batch size was set to 32. The CNN experiments used a 5-fold cross-validation scheme, so the image collection was randomly partitioned into five folds of 198–199 images each. In each training, four folds constituted a set of ca. 800 images for training and validation (split with a 15:1 ratio). We took care to distribute the data from three source datasets across folds. To avoid overfitting, we applied selected data augmentation procedures to the training set: random horizontal and vertical translation by max. ± 20 pixels, random rotation by max. $\pm 5°$, and a horizontal flip with a 50% probability.

The CNN outcome is subjected to a series of corrections using morphological operations: reconstruction using the starting point and 8-connectivity, filling of holes, and morphological closing with a small kernel to smooth the edges. A resulting binary mask is then passed to the active contour analysis in the postprocessing stage.

Active contour postprocessing

To adjust the CNN segmentation result, we prepared postprocessing procedures based mainly on the active contour evolution. With the main stage outcome determining the initial contour, we tested two models: geodesic active contour (GAC)[39] and the Chan-Vese model[40]. The former involves edge detection to trace object boundaries, while the latter uses level sets to handle objects with discontinued or blurred edges. The contour energy minimization during evolution is controlled by two main parameters: contraction bias *CB* and smooth

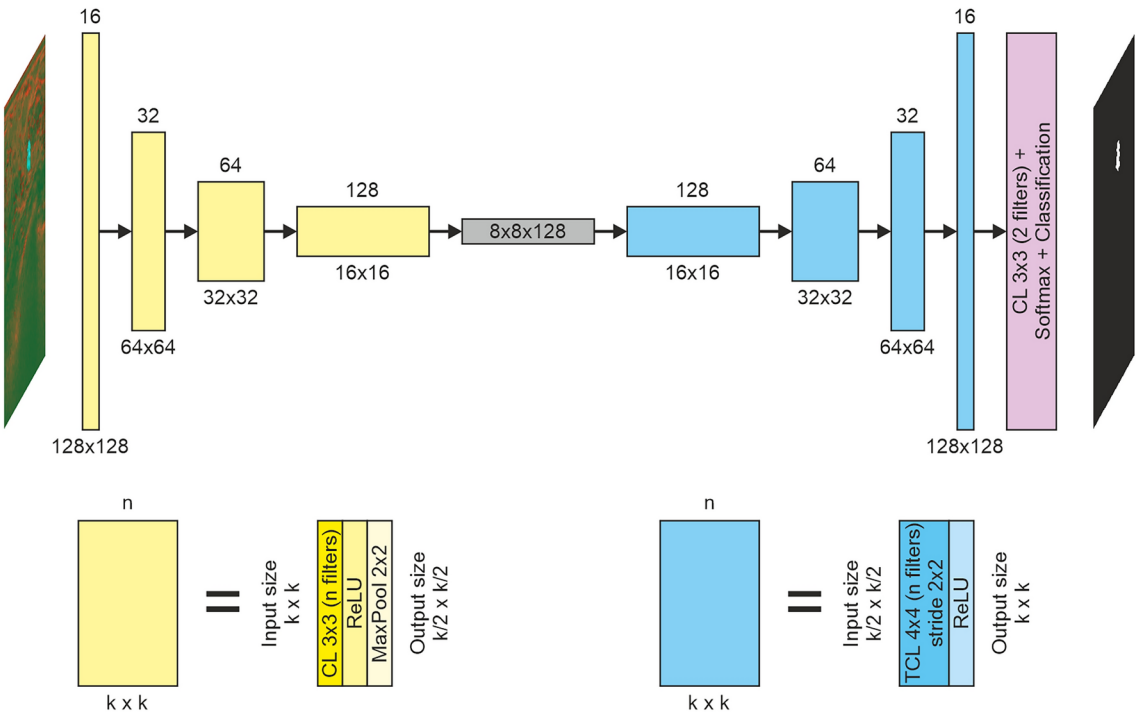

Fig. 4. Autoencoder CNN architecture for breast tumor segmentation. CL – convolutional layer, TCL – transposed CL.

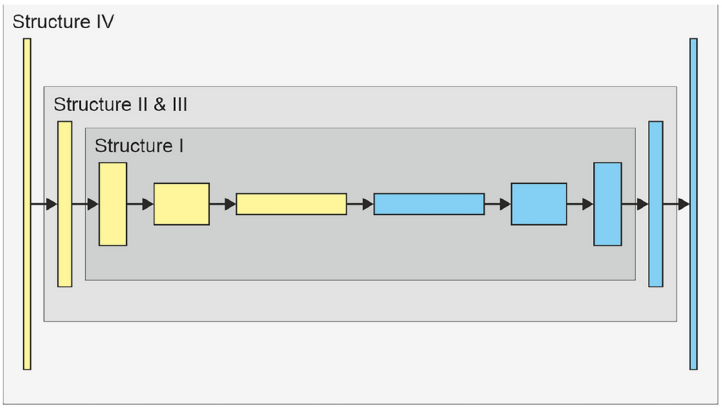

Structure	Depth	No. of filters	No. of parameters
I	3	16–…–64	318,786
II	4	16–…–128	531,890
III	4	32–…–256	1,085,010
IV	5	16–…–256	2,138,034

Fig. 5. Illustration of various CNN architectures verified in the study.

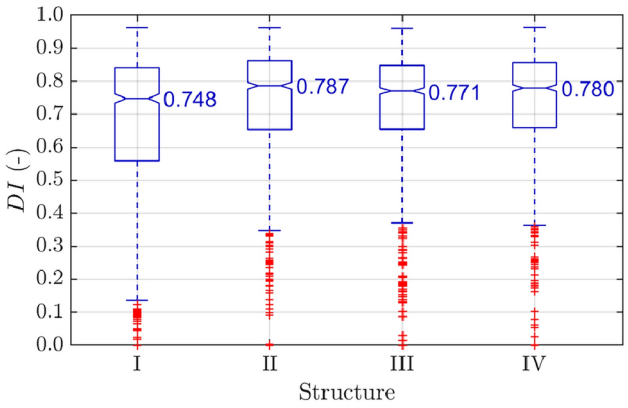

Fig. 6. Results of the CNN architecture analysis. Each box covers the interquartile range (IQR) with a median given and indicated by a central line. Whiskers refer to $1.5 \cdot \mathrm{IQR}$. Outliers are shown with red points.

factor *SF*. A detailed analysis of their influence on the segmentation performance, along with ultimate settings, is provided in "Active contour analysis" Section.

The binary mask resulting from the contour evolution is subjected to a sequence of morphological operations similar to those applied to the CNN outcome (morphological reconstruction, filling holes, morphological closing), yielding the final result of breast lesion segmentation.

Results and discussion

The Dice index *DI* was used to assess the segmentation performance in each image:

$$DI = \frac{2 \cdot TP}{2 \cdot TP + FP + FN}, \tag{7}$$

where *TP*, *FP*, and *FN* denote the number of true positive, false positive, and false negative pixels, respectively. The Dice similarity coefficient is a universal measure for validating segmentation algorithms due to its high reliability in estimating spatial overlap, especially in small objects.

The results of individual experiments were aggregated and presented in various forms. The following sections describe four experiments on the segmentation settings (both CNN and AC) and a comparative analysis regarding recent state-of-the-art solutions.

CNN architecture

We verified four variants of the autoencoder CNN architecture to justify the selection presented in "CNN segmentation" Section. The networks differed in depth and number of convolutional filters. Figure 5 illustrates and specifies the models. The number of trainable parameters approximately doubles in subsequent architectures. Note that the model presented in Fig. 4 refers to structure II.

Figure 6 presents the *DI* box plots of the main stage outcome, with selected statistical measures given in Table 1. While the shallow model I is clearly the least effective, the other three structures do not differ significantly in *DI* measures. Several factors point to structure II: the highest median and third quartile of the Dice index and

Structure	Q1	Median	Q3	Mean ± std
I	0.559	0.748	0.842	0.661 ± 0.242
II	0.654	0.787	0.862	0.724 ± 0.200
III	0.655	0.771	0.848	0.718 ± 0.195
IV	0.659	0.780	0.856	0.729 ± 0.186

Table 1. Results of the CNN architecture analysis. Q1, Q3 – first and third quartile, respectively.

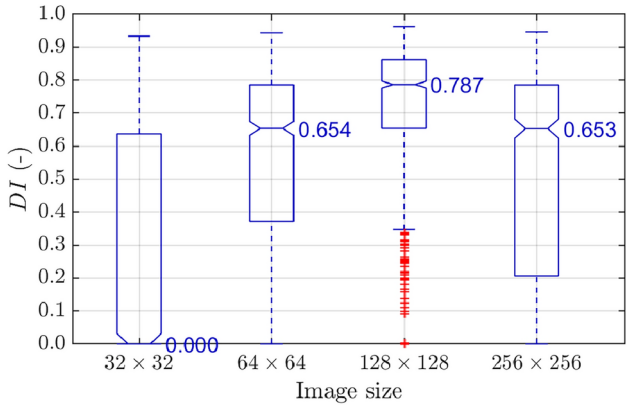

Fig. 7. Results of the input image resolution analysis. Each box covers the interquartile range (IQR) with a median given and indicated by a central line. Whiskers refer to $1.5 \cdot \mathrm{IQR}$. Outliers are shown with red points.

Image size	Q1	Median	Q3	Mean ± std
32×32	0.000	0.000	0.638	0.271 ± 0.339
64×64	0.371	0.654	0.786	0.543 ± 0.309
128×128	0.654	0.787	0.862	0.724 ± 0.200
256×256	0.206	0.653	0.786	0.518 ± 0.326

Table 2. Results of the input image resolution analysis. Q1, Q3 – first and third quartile, respectively.

the smallest capacity, lowering memory and processing time requirements compared to structures III and IV. Thus, we incorporated structure II into the segmentation workflow.

Input image resolution

With the selected network structure, we investigated the impact of the input image resolution on the main-stage segmentation results. Four image sizes were analyzed: 32×32, 64×64, 128×128, and 256×256 pixels. Figure 7 shows the *DI* box plots, and Table 2 contains selected *DI* statistical measures over the aggregated set. A zero *DI* median excludes the 32×32 option, though high values were obtained in isolated cases even with such a small image. The 64×64 size produces a median *DI* of 0.65 but with a relatively sizeable interquartile range. Top results are obtained with a resolution of 128×128 pixels (the highest median at 0.79 and both quartiles, the smallest interquartile range). The value of Q1 is at the median level for 64×64 and 256×256. Thus, the image size of 128×128 pixels is optimal for segmentation. Larger images only increase the computational power requirements without improved performance.

GradCAM evaluation

Apart from quantitative evaluation, we aimed to provide a qualitative assessment of the CNN segmentation results by employing the gradient-weighted class activation mapping (Grad-CAM) algorithm[41,42]. As an interpretable artificial intelligence (XAI) tool, its goal is to indicate image parts having the most significant impact on deep model inference. Such an analysis verifies whether irrational factors do not cause the network's decision. Figure 8 shows the GradCAM mapping results for the network's last layer in sample images from our dataset. In each case, pixels in the middle of the lesion (white&yellow) are most important for segmentation, while those at the edges (red) contribute less. The GradCAM maps indicate that the network focuses on lesion areas, which would likely attract the expert's attention in clinical conditions.

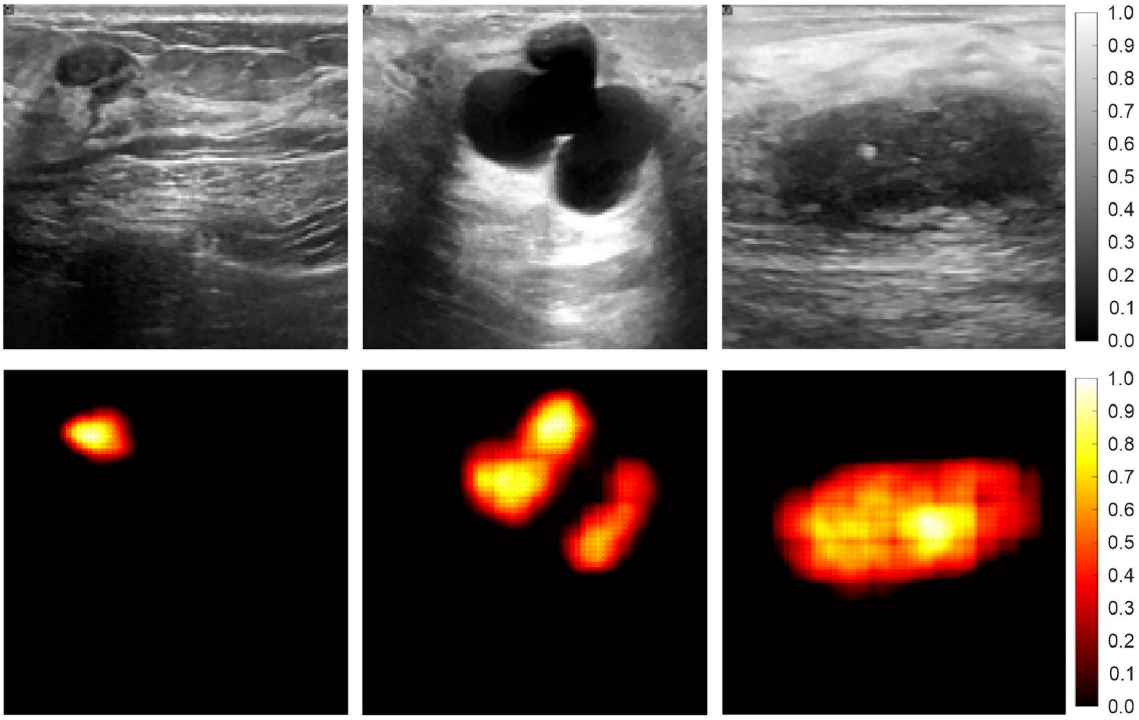

Fig. 8. Illustration of GradCAM mapping (bottom row) in three cases from the dataset (top row).

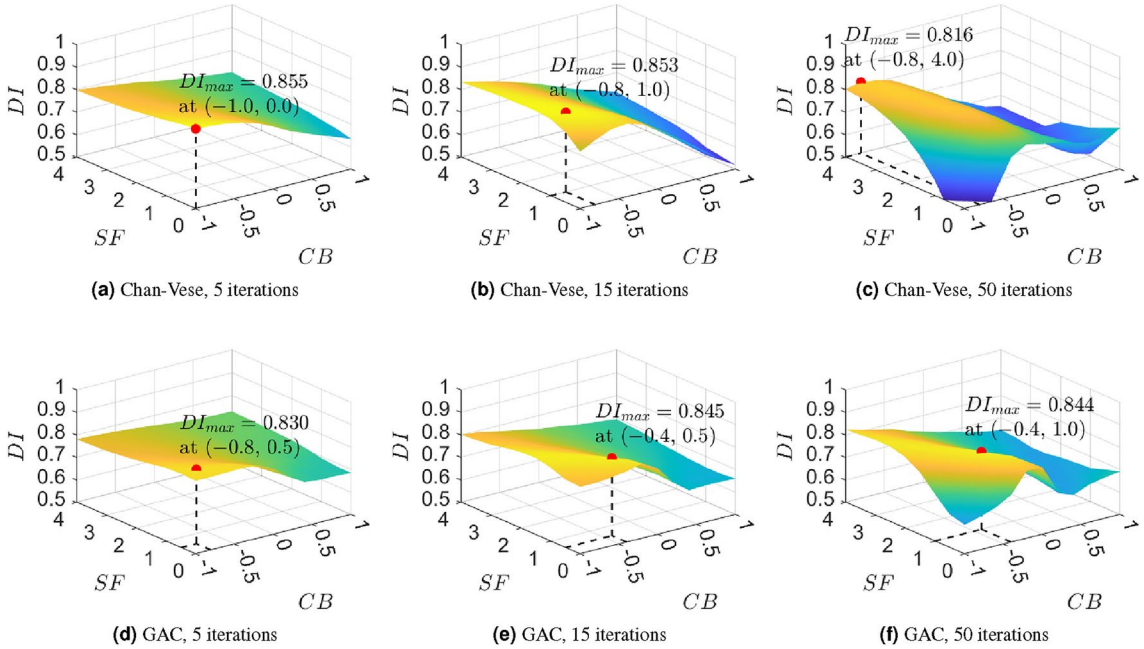

(a) Chan-Vese, 5 iterations **(b)** Chan-Vese, 15 iterations **(c)** Chan-Vese, 50 iterations

(d) GAC, 5 iterations **(e)** GAC, 15 iterations **(f)** GAC, 50 iterations

Fig. 9. Median *DI* distribution in the 5th, 15th, and 50th iteration of the active contour evolution as a function of *CB* and *SF*. Left: Chan-Vese model, right: GAC model. The red marker indicates the *DI* maximum in each chart.

Active contour analysis

The experiments on the active contour part of the workflow involved investigating four settings: the Chan-Vese vs. GAC model selection, contraction bias *CB*, smooth factor *SF*, and the number of evolution iterations. We verified the evolution of the initial contour, as described in "Active contour postprocessing" Section.

Figure 9 shows the results of the grid-search evaluation with *CB* ranging from -1.0 to 1.0 and *SF* from 0.0 to 4.0 in both Chan-Vese model (top row) and GAC (bottom row). The median surfaces correspond to the

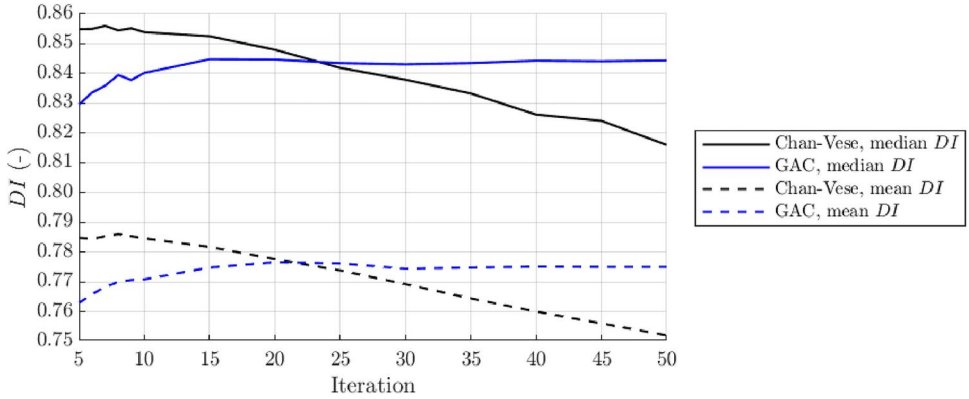

Fig. 10. Plots of mean and median *DI* over iterations of the active contour evolution in the Chan-Vese and GAC models.

Method	Description	Data	Average *DI*		
			BUSI	Dataset B	OASBUD
Huang et al.[27].	SCFURNet model	1830 images, 4 datasets incl. BUSI and Dataset B	0.81	0.81	–
Lu et al.[28].	HAG-Net model	980 images, 2 datasets: BUSI and OASBUD	0.83	–	0.78
Chen et al.[29].	RRCNet model	943 images, 2 datasets: BUSI and Dataset B	0.79	0.80	–
Yang et al.[30].	CSwin-PNet model	943 images, 2 datasets: BUSI and Dataset B	0.84	0.87	–
Ru et al.[31].	Att-U-Node model	1180 images, 5 datasets incl. BUSI, Dataset B, and OASBUD	0.77	0.78	0.60
Our model	FC + CNN + AC	993 images, 3 datasets: BUSI, Dataset B, and OASBUD	0.79		

Table 3. Comparison of the proposed method and the state-of-the-art in breast tumor segmentation. The rightmost column shows only the results obtained over three public datasets used in this study.

median *DI* in the 5th, 15th, and 50th iterations. The maximum median *DI*s with the argument values are given on each surface. With a small number of iterations, the surface resembles a plane. With the ongoing evolution, the impact of contour parameters becomes more meaningful. Both models perform best with a negative *CB* (outward expansion trend). The *SF*'s impact depends on the stage of evolution in the Chan-Vese model, while in the GAC, it should not exceed 1.0. The median Dice index is the highest (above 0.85) in the early Chan-Vese evolution stages and decreases significantly after the 15th iteration. On the contrary, in GAC, it slightly increases at the beginning and stabilizes at ca. 0.845. To confirm this observation, note Fig. 10, which shows the top median and mean Dice index in iterations 5–50.

Based on the above experiments, we selected the Chan-Vese model with $CB = -0.6$, $SF = 4.0$, and seven iterations, yielding a median *DI* of 0.856 and a mean *DI* of 0.786.

Comparison to the state-of-the-art

Table 3 shows our results compared to the existing solutions described in "Introduction" Section. For comparison, we selected only methods (1) described in the last two years (2022-2023) in recognized sources, (2) trained or tested using at least two of the three public US image databases used in this study[27–31](only Ru et al.[31] employed all three databases). All methods rely on deep neural networks with architectures usually deeper and more advanced than those proposed in this paper; all apply the testing strategy within single databases. Table 3 presents all reported average *DI* measures.

In reference methods, the Dice index in individual databases ranges from 0.60 to 0.87. Among them, the model of Yang et al. published in March 2023[30] stands out, based on a transformer-type network ($DI = 0.84$ and 0.87). However, Yang's method was not tested using the OASBUD database. The analysis of Table 3 indicates that the results obtained in OASBUD are significantly worse than in other databases, suggesting it is more difficult in the analysis ($DI = 0.6$ in Ru et al.[31] and 0.78 in Lu et al.[28]). Since we combine the databases in training and testing, the OASBUD cases can influence the performance of our method. Results from Ru et al.[31] over all three datasets can be a fair benchmark; our average Dice index of 0.79 (median of 0.86) is better than Ru's results, proving our method's competitiveness.

Discussion

Apart from the experimental results already discussed in this section, we want to focus on several issues and limitations of our study.

Although fuzzy connectedness is a relatively well-established tool in image segmentation, its incorporation into frameworks based on deep networks is not frequent. Available approaches place the FC module in different stages of the workflow, e.g., after the deep analysis[43]or next to it[44]. The general idea of combining multiple image representations or adjacent scans in a single, three-dimensional input structure is not new. However, to our knowledge, the FC analysis was not used to prepare input data for the deep model. As fuzzy connectivity brings valuable information on texture and semantics within the image topology, we find it a vital contribution to supporting the original data. Original works on fuzzy affinity[42] featured a variety of opportunities to customize FC calculations. Since then, a lot of research has been done on this matter. We propose a distance-related fuzzy affinity component and produce different weight combinations to determine connectivity maps driven by particular image specifics. We placed the fuzzy connectivity scenes in chromatic channels of a pseudo-RGB image next to the original scan. In the experiments, we investigated constructing a 3D input matrix of more than three layers with even more FC scenes in various configurations. Still, the three-channel pseudo-RGB approach turned out to be sufficiently effective. Since there are no contradictions to applying this idea to different tasks or image modalities, we leave it for further consideration.

The autoencoder-type model we use is relatively shallow. However, the experiments in "CNN architecture" Section justify the architecture settings. Note that the mean Dice index of 0.79 obtained by the method falls within the range reported in individual benchmark collections (0.60–0.87) by most up-to-date studies from 2022–2023[27–31]. Our model was trained and validated over a combined database, making it more robust and insensitive to the variability of data sources, acquisition equipment and parameters, and expert delineation specifics. The above conclusion comes from a comparison to the study of Ru et al.[31], the only one that used all three databases under consideration (our 0.79 vs. Ru's 0.60–0.78). Thus, the simplicity of the network turns into an advantage due to a small number of parameters, limiting computational requirements.

We would like to mention the limitations of this study. The FC method is generally semi-automated as it requires providing seed points. In many applications, some basic level of interaction is required from the user. However, the seed points can result from initial processing, e.g., detection of a single pixel within the object or coarse presegmentation. Note that FC does not necessarily accept single seeds but can be supplied with sets of points without a problem for the mathematical apparatus. Therefore, any initial binary mask is acceptable. The method can be equipped with the initial detection of the lesion center to fully automate the algorithm. Consider also extending our 2D segmentation method into the third dimension, the time domain in US imaging. The US continuously records frames to be collected in a video stream, where successive projections are very similar. A single seed point can lead to segmenting the lesion in the first scan. In such a case, the seeds for consecutive frames can easily be determined automatically based on previous results. Even if the first seed point is required in such a framework, it is an acceptable level of interaction for the analysis of diagnostic video sequences. We can also mention the image database size. We are aware that deep networks generally learn better with more than a thousand images. In our study, the problem was addressed through data augmentation. However, note that the number of images is typical for this task[24–31]. No collections exist that would extend the amount of data to make a significant difference. Finally, the active contour procedure seems the most vulnerable to the challenging appearance of breast lesions in US. In some cases, the object edge discontinuities confuse the AC. We paid particular attention to adjusting the AC settings to the combined and diversified dataset and significantly improved the segmentation in postprocessing ("Active contour analysis" Section). Nevertheless, this stage deserves further analysis with every new reference data available.

At that point, the method is ready for further development, including the next stages of breast cancer CAD. For instance, robust segmentation provides a basis for texture analysis and possible malignancy assessment. With access to a time series of continuous US frames captured under the optical tracking system, we also consider employing our methodology to reconstruct and measure 3D tumor volume. Preliminary studies involving biopsy phantoms are promising for accurate navigation perspectives.

Conclusion

The hybrid workflow presented in this paper offers efficient breast tumor segmentation in ultrasound, validated over a diverse collection from public sources. We propose a modified fuzzy connectedness approach based on a novel distance-related fuzzy affinity component to prepare data for the autoencoder deep neural network and then adjust the segmentation with an active contour. We produce different weight combinations to determine fuzzy connectivity maps driven by particular image specifics. As fuzzy connectivity brings valuable information on texture and semantics within the image topology, we find it a vital contribution to supporting the original data. Apart from the specific scope and application in breast cancer diagnosis, we believe this study may spark a discussion on the benefits of fuzzy connectedness for deep analysis of biomedical images.

Data availibility

Two datasets analyzed during the current study are available in the BUSI repository https://doi.org/10.1016/j.dib.2019.104863 and the OASBUD http://bluebox.ippt.gov.pl/%7ehpiotrzk/download.html. The third dataset (Dataset B) used and analyzed during the current study is available from the corresponding author of the cited paper https://doi.org/10.1117/1.JMI.6.1.011007.

Received: 19 June 2024; Accepted: 14 October 2024
Published online: 28 October 2024

References

1. Jemal, A. et al. Global cancer statistics. *CA Cancer J. Clin.* **61**, 69–90. https://doi.org/10.3322/caac.20107 (2011).

2. American Cancer Society. Breast cancer facts and figures 2022-2024. https://www.cancer.org/research/cancer-facts-statistics/breast-cancer-facts-figures.html (2022). [Online; accessed 02.08.2023].
3. Centers for Disease Control and Prevention (CDC). What Is Breast Cancer? https://www.cdc.gov/cancer/breast/basic_info/what-is-breast-cancer.htm (2021). [Online; accessed 02.08.2023].
4. Scully, O. J., Bay, B.-H., Yip, G. & Yu, Y. Breast cancer metastasis. *Cancer Genom. Proteom.* **9**, 311–320 (2012).
5. Wojciechowska, U. et al. *Malignant cancers in Poland in 2020, (PL) Nowotwory złośliwe w Polsce w 2020 roku* (National Cancer Registry, PL) Krajowy Rejestr Nowotworów, Warszawa, 2022).
6. Jassem, J. & Krzakowski, M. Rak piersi. *Oncoly in Clinical Practice—Education, (PL) Onkologia w Praktyce Klinicznej—Edukacja* **4**, 209–256 (2018).
7. Wesołowska, E. *Fundamentals of Clinical Oncology, Screening for Early Detection of Breast Cancer, (PL) Podstawy onkologii klinicznej, Badania przesiewowe w zakresie wczesnego wykrywania raka piersi*, chap. 2, 17–20 (Centrum Medyczne Ksztalcenia Podyplomowego w Warszawie,) (2011).
8. Bock, K. et al. Pathologic breast conditions in childhood and adolescence: evaluation by sonographic diagnosis. *J. Ultrasound Med.* **24**, 1347–1354. https://doi.org/10.7863/jum.2005.24.10.1347 (2005).
9. Ślubowski, T., Ślubowska, M. & Wojciechowski, A. Diagnostic techniques in breast cancer detection. part i: Imaging methods and their modifications. *Ginekologia Polska* **78** (2007).
10. Chan, V. & Perlas, A. Basics of ultrasound imaging. In *Atlas of ultrasound-guided procedures in interventional pain management*, 13–19, https://doi.org/10.1007/978-1-4419-1681-5_2 (Springer, 2011).
11. Makuuchi, M., Torzilli, G. & Machi, J. History of intraoperative ultrasound. *Ultrasound Med. Biol.* **24**, 1229–1242. https://doi.org/10.1016/S0301-5629(98)00112-4 (1998).
12. Colakovic, N. et al. Intraoperative ultrasound in breast cancer surgery from localization of non-palpable tumors to objectively measurable excision. *World J. Surg. Oncol.* **16**, 1–7. https://doi.org/10.1186/s12957-018-1488-1 (2018).
13. Helbich, T., Matzek, W. & Fuchsjäger, M. Stereotactic and ultrasound-guided breast biopsy. *Eur. Radiol.* **14**, 383–393. https://doi.org/10.1007/s00330-003-2141-z (2004).
14. Pyciński, B. *et al.* Image guided core needle biopsy of the breast. In *International Conference on Information Technologies in Biomedicine*, 160–171, https://doi.org/10.1007/978-3-319-91211-0_14 (Springer, 2018).
15. Czajkowska, J., Pyciński, B., Juszczyk, J. & Pietka, E. Biopsy needle tracking technique in US images. *Comput. Med. Imaging Graphics* **65**, 93–101. https://doi.org/10.1016/j.compmedimag.2017.07.001 (2018).
16. Yadav, N., Dass, R. & Virmani, J. Objective assessment of segmentation models for thyroid ultrasound images. *J. Ultrasound* **26**, 673–685. https://doi.org/10.1007/s40477-022-00726-8 (2022).
17. Pham, D. L., Xu, C. & Prince, J. L. Current methods in medical image segmentation. *Ann. Rev. Biomed. Eng.* **2**, 315–337. https://doi.org/10.1146/annurev.bioeng.2.1.315 (2000).
18. Litjens, G. et al. A survey on deep learning in medical image analysis. *Med. Image Anal.* **42**, 60–88. https://doi.org/10.1016/j.media.2017.07.005 (2017).
19. Minaee, S. et al. Image segmentation using deep learning: A survey. *IEEE Trans. Pattern Anal. Machine Intell.* **44**, 3523–3542. https://doi.org/10.1109/TPAMI.2021.3059968 (2022).
20. Al-Dhabyani, W., Goma, M., Khaled, H. & Fahmy, A. Dataset of breast ultrasound images. *Data in Brief* **28**, https://doi.org/10.1016/j.dib.2019.104863 (2020).
21. Muhammad, M., Zeebaree, D., Brifcani, A. M. A., Saeed, J. & Zebari, D. A. Region of interest segmentation based on clustering techniques for breast cancer ultrasound images: A review. *J. Appl. Sci. Technol. Trends* **1**, 78–91, https://doi.org/10.38094/jastt20201328 (2020).
22. Huang, Q., Luo, Y. & Zhang, Q. Breast ultrasound image segmentation: a survey. *Int. J. Comput. Assist. Radiol. Surg.* **12**, 493–507. https://doi.org/10.1007/s11548-016-1513-1 (2017).
23. Kriti, Virmani, J. & Agarwal, R. Assessment of despeckle filtering algorithms for segmentation of breast tumours from ultrasound images. *Biocybernetics Biomed. Eng.* **39**, 100–121, https://doi.org/10.1016/j.bbe.2018.10.002 (2019).
24. Almajalid, R., Shan, J., Du, Y. & Zhang, M. Development of a deep-learning-based method for breast ultrasound image segmentation. In *2018 17th IEEE International Conference on Machine Learning and Applications (ICMLA)*, 1103–1108, https://doi.org/10.1109/ICMLA.2018.00179 (2018).
25. Vakanski, A., Xian, M. & Freer, P. E. Attention-enriched deep learning model for breast tumor segmentation in ultrasound images. *Ultrasound Med. Biol.* **46**, 2819–2833. https://doi.org/10.1016/j.ultrasmedbio.2020.06.015 (2020).
26. Shareef, B., Xian, M. & Vakanski, A. Stan: Small tumor-aware network for breast ultrasound image segmentation. In *2020 IEEE 17th International Symposium on Biomedical Imaging (ISBI)*, 1–5, https://doi.org/10.1109/ISBI45749.2020.9098691 (2020).
27. Huang, K., Zhang, Y., Cheng, H.-D. & Xing, P. Trustworthy breast ultrasound image semantic segmentation based on fuzzy uncertainty reduction. *Healthcare* **10**, https://doi.org/10.3390/healthcare10122480 (2022).
28. Lu, Y. et al. A hybrid attentional guidance network for tumors segmentation of breast ultrasound images. *Int. J. Comput. Assist. Radiol. Surg.*[SPACE]https://doi.org/10.1007/s11548-023-02849-7 (2023).
29. Chen, G., Dai, Y. & Zhang, J. RRCNet: Refinement residual convolutional network for breast ultrasound images segmentation. *Eng. Appl. Artif. Intell.* **117**, 105601. https://doi.org/10.1016/j.engappai.2022.105601 (2023).
30. Yang, H. & Yang, D. CSwin-PNet: A CNN-Swin transformer combined pyramid network for breast lesion segmentation in ultrasound images. *Exp. Syst. Appl.* **213**, 119024. https://doi.org/10.1016/j.eswa.2022.119024 (2023).
31. Ru, J. et al. Attention guided neural ODE network for breast tumor segmentation in medical images. *Comput. Biol. Med.* **159**, 106884. https://doi.org/10.1016/j.compbiomed.2023.106884 (2023).
32. Yap, M. *et al.* Breast ultrasound lesions recognition: end-to-end deep learning approaches. *J. Med. Imaging* **6**, https://doi.org/10.1117/1.JMI.6.1.011007 (2018).
33. Piotrzkowska-Wróblewska, H., Dobruch-Sobczak, K., Byra, M. & Nowicki, A. Open access database of raw ultrasonic signals acquired from malignant and benign breast lesions. *Med. Phys.* **44**, https://doi.org/10.1002/mp.12538 (2017).
34. Zhang, Y. et al. BUSIS: A benchmark for breast ultrasound image segmentation. *Healthcare* **10**, 729. https://doi.org/10.3390/healthcare10040729 (2022).
35. Udupa, J. K. & Samarasekera, S. Fuzzy connectedness and object definition: Theory, algorithms, and applications in image segmentation. *Graph. Models Image Process.* **58**, 246–261. https://doi.org/10.1006/gmip.1996.0021 (1996).
36. Udupa, J. & Saha, P. Fuzzy connectedness and image segmentation. *Proc. IEEE* **91**, 1649–1669. https://doi.org/10.1109/jproc.2003.817883 (2003).
37. Saha, P. K., Udupa, J. K. & Odhner, D. Scale-based fuzzy connected image segmentation: Theory, algorithms, and validation. *Comput. Vision Image Understand.* **77**, 145–174. https://doi.org/10.1006/cviu.1999.0813 (2000).
38. Badura, P., Kawa, J., Czajkowska, J., Rudzki, M. & Pietka, E. Fuzzy connectedness in segmentation of medical images: A look at the pros and cons. In Rosa, A., Kacprzyk, J., Filipe, J. & Correia, A. (eds.) *ECTA 2011 FCTA 2011 - Proceedings of the International Conference on Evolutionary Computation Theory and Applications and International Conference on Fuzzy Computation Theory and Applications*, 486–492, https://doi.org/10.5220/0003670904860492 (2011).
39. Caselles, V., Kimmel, R. & Sapiro, G. Geodesic active contours. *Int. J. Comput. Vision* **22**, 61–79. https://doi.org/10.1023/A:1007979827043 (1997).
40. Chan, T. F. & Vese, L. A. Active contours without edges. *IEEE Trans. Image Process.* **10**, 266–277. https://doi.org/10.1109/83.902291 (2001).

41. Selvaraju, R. R. *et al.* Grad-CAM: Visual explanations from deep networks via gradient-based localization. In *Proceedings of the IEEE International Conference on Computer Vision (ICCV)*, 618–626, https://doi.org/10.1007/s11263-019-01228-7 (2017).
42. Vinogradova, K., Dibrov, A. & Myers, G. Towards interpretable semantic segmentation via gradient-weighted class activation mapping (student abstract). *Proc. AAAI Conf. Artif. Intell.* **34**, 13943–13944. https://doi.org/10.1609/aaai.v34i10.7244 (2020).
43. Czajkowska, J., Badura, P., Korzekwa, S. & Płatkowska-Szczerek, A. Automated segmentation of epidermis in high-frequency ultrasound of pathological skin using a cascade of DeepLab v3+ networks and fuzzy connectedness. *Comput. Med. Imaging Graphics* **95**, 102023. https://doi.org/10.1016/j.compmedimag.2021.102023 (2022).
44. Bai, P. et al. A novel framework for improving pulse-coupled neural networks with fuzzy connectedness for medical image segmentation. *IEEE Access* **8**, 138129–138140. https://doi.org/10.1109/ACCESS.2020.3012160 (2020).

Acknowledgements

This research was supported partially by the European Funds for Silesia 2021–2027 Program co-financed by the Just Transition Fund Project "Development of the Silesian Biomedical Engineering Potential in the Face of the Challenges of the Digital and Green Economy (BioMeDiG)" under Grant FESL.10.25-IZ.01-07G5/23 and partially by the Polish Ministry of Science and Education and Silesian University of Technology statutory financial support No. 07/010/BK_24/1034.

Author contributions

All authors are justifiably credited with authorship. The detailed contribution is as follows: M.B. – conceptualization, methodology, software, validation, investigation, resources, data curation, writing—original draft, visualization; J.J. – conceptualization, formal analysis, writing—review & editing, project administration, funding acquisition; P.B. – conceptualization, validation, formal analysis, writing—original draft, visualization, supervision, funding acquisition.

Declarations

Competing interests

The authors declare no competing interests.

Additional information

Correspondence and requests for materials should be addressed to M.B.

Reprints and permissions information is available at www.nature.com/reprints.

Publisher's note Springer Nature remains neutral with regard to jurisdictional claims in published maps and institutional affiliations.